Soft Matter

Enhanced water-responsive actuation of porous Bombyx mori silk

Journal:	*Soft Matter*
Manuscript ID	SM-COM-12-2022-001601.R2
Article Type:	Communication
Date Submitted by the Author:	16-Feb-2023
Complete List of Authors:	Jung, Yeojin; CUNY Advanced Science Research Center Khan, Maheen; CUNY Advanced Science Research Center Podbevsek, Darjan; CUNY ASRC, Sudhakar, Tejaswini; The City College of New York Tu, Raymond; The City College of New York, Chemical Engineering Chen, Xi; CUNY Advanced Science Research Center,

COMMUNICATION

Enhanced water-responsive actuation of porous *Bombyx mori* silk†

SReceived 00th January 20xx,
Accepted 00th January 20xx

DOI: 10.1039/x0xx00000x

Yeojin Jung,[ab] Maheen K. Khan,[ab] Darjan Podbevšek,[b] Tejaswini Sudhakar,[c] Raymond S. Tu,*[ab] Xi Chen,*[abd]

***Bombyx mori* silk with nanoscale porous architecture significantly deforms in response to changes in relative humidity. Despite the increasing amount of water adsorption and water-responsive strain with increasing porosity of silk, there is a range of porosities that result in silk's optimal water-responsive energy density at 3.1 MJ m^{-3}. Our findings show the possibility of controlling water-responsive materials' swelling pressure by controlling their nanoporosities.**

Water-responsive (WR) materials have been recently shown to generate higher actuation energy per unit volume over natural muscles and conventional actuators when they deform in response to changes in relative humidity (RH)[1–3]. These studies suggest the potential of using WR materials as actuating components for a wide range of engineering applications, including robotics[4], shape morphing[5], smart structures[6], and new kinds of evaporation energy harvesting systems[7]. However, the design criteria that systematically yield high-performance WR materials is still not fully understood, limiting the development and scaling up of silk as an emerging actuator material.

One common feature of high-performance WR materials developed in nature, such as cellulose-[8–10] and protein-based[11,12] WR materials, is that they often consist of hierarchical and stiff architectures with pores at nanometer scale[2,11]. For instance, a recent study showed that *Bacillus subtilis* cell wall peptidoglycan possesses a rigid (1.7 GPa - 4.5 GPa Young's modulus) and hierarchical structure with nanoscale pores (~6.8 nm - 38.4 nm in diameter) and shows a record-high WR energy density of 72.6 MJ m^{-3}, surpassing those of existing actuator materials and muscles[2]. By incorporating stiff domains and nanoporous structures, researchers have developed a number of synthetic materials, such as metal-organic frameworks-based composites[13,14], Nafion-based films[15,16], sol-gel silica films[17], nanoprous metals[18], titanium oxide nanotube films[19,20], and polyethylenimine/poly(acrylic acid) films[21], which all possess significant WR actuation. For instance, titanium oxide nanotube films with ~100 nm pores show a high energy density of ~1250 kJ m^{-3} [20]. These studies suggest that mechanical properties and nanoporosity are critical to materials' water-responsiveness[12–17].

In our previous study, we demonstrated that *Bombyx (B.) mori* silk's WR energy can be dramatically increased from 0.2 to 1.6 MJ m^{-3} by increasing silk's mechanical stiffness[1] or adding stiff silica nanoparticles[22]. It is clear that, during WR actuation, the materials' high stiffness can help effectively translate chemical potential of water into work performed on external loads. However, there is still a lack of knowledge on the effect of porous structures on materials' water-responsiveness. In this study, we use *B. mori* silk as a platform to further investigate the effect of porosity on water-responsiveness. Given the significant capillary stress with pore sizes on the nanometer length scale[18], together with the pore structures where high-performance WR actuation is observed[15,17,20], we hypothesize that porous silk with nanometer scale pores can exhibit high WR energy density and silk's WR actuation can be controlled by varying porosity. Based on this hypothesis, we used an established method where water-soluble poly(ethylene oxide) (PEO) is used as a sacrificial materials to systematically vary silk's porosity[23–27].

The regenerated silk fibroin aqueous solution was first prepared by following protocols described in Jung et al.[22]. *B. mori* raw silk

[a] *Department of Chemical Engineering, The City College of New York, 160 Convent Avenue, New York, NY 10031, USA*
[b] *Advanced Science Research Center (ASRC) at the Graduate Center, City University of New York, 85 St. Nicholas Terrace, New York, NY 10031, USA*
[c] *Department of Biomedical Engineering, The City College of New York, 160 Convent Avenue, New York, NY 10031, USA*
[d] *Ph.D. Program in Chemistry and Physics, The Graduate Center of the City University of New York, 365 Fifth Avenue, New York, NY 10016, USA*
Email: xchen@gc.cuny.edu, tu@ccny.cuny.edu
† Electronic Supplementary Information (ESI) available.
See DOI: 10.1039/x0xx00000x

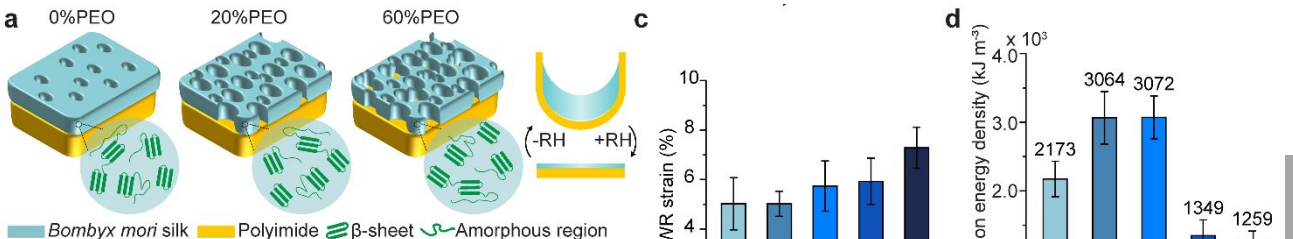

cocoons (TTSAM) were cut into small pieces that were then boiled in a 0.02 M aqueous sodium carbonate (Sigma-Aldrich) solution for 30 min and rinsed thoroughly three times in ultrapure water for 20 min to remove glue-like sericin proteins. After drying, the silk pieces were dissolved in a 9.3 M aqueous lithium bromide (LiBr, Fisherbrand) solution with a ratio of 0.25 g silk to 1 mL LiBr (250 g/L) at 60 °C for 2 h. Then, the dissolved silk fibroin was dialyzed in ultrapure water to remove LiBr ions using cellulose dialysis tubing (molecular weight cut-off is 3,500 Daltons, Fisherbrand) for 2 h, and the dialyzed material was centrifuged at 6973 G for 20 min. The regenerated silk solution yielded a concentration of ~10 wt%, which was determined by weighing the remaining solid silk after drying.

To vary regenerated silk's porosity, we selected PEO with an average molecular weight of 900,000 g/mol (Sigma-Aldrich) that was previously reported to generate nanoporous geometries with the pore size of ~100 nm[27]. First, 1.87 µL of regenerated silk and 2 wt% PEO solutions were mixed to prepare solutions with various PEO concentrations from 0 vol% to 60 vol%. (0 vol%, 0%PEO; 10 vol%, 10%PEO; 20 vol%, 20%PEO; 40 vol%, 40%PEO; 60 vol%, 60%PEO). The silk/PEO blends were then cast on a Mylar film, dried overnight inside a humid chamber (~90% RH) at room temperature allowing the formation of silk films with a relatively uniform thickness. The dried silk films were subsequently peeled off to form freestanding films. The solutions were also deposited on 3 mm x 4 mm x 25 µm thin polyimide films (CAPLINQ), which were pre-treated by plasma (M 1070 NanoClean, Fischione) for 30 sec, to form bilayer structures. The silk/PEO coated films were then dried overnight inside a humid chamber (~90% RH) at room temperature to form bilayer structures. Both freestanding and bilayer films were immersed in a 99.9% methanol solution (Sigma-Aldrich) for 10 min. After the methanol treatment, silk/PEO films were immersed in ultrapure water for one day to remove PEO[25], and were allowed to dry to form porous silk (Figure 1a).

These regenerated, porous silk show distinct water-responsive behavior (Figure 1b). To characterize silk's WR strain, silk freestanding films (3 mm x 10 mm x 10 µm) were placed inside a section of rigid plastic tubing where RH is changed between 10% and 90% by flowing dry or humid air. The WR strain is defined as a ratio of deformation (the change in length in response to 10% and 90% RH) to the film's original length, determined by ImageJ software, during the reversible linear contraction/expansion upon three RH cycles (Figure S1, ESI†). Figure 1c shows a slight increase in the WR strain of the silk with increasing volume fraction of PEO: 5.02% (±1.05) for 0%PEO, 5.02% (±0.51) for 10%PEO, 5.74% (±1.01) for 20%PEO, 5.93% (±0.93) for 40%PEO, and 7.29% (±0.83) for 60%PEO, which could be attributed to the increasing porosity of silk.

The WR speed and energy densities of porous silk were determined from WR actuation of silk/polyimide bilayer films. To investigate, silk/polyimide bilayers were placed inside a chamber, where RH is alternated between 10% and 90% by supplying humid and dry air. We noted that all silk/polyimide bilayer films took similar time to bend within 13-44 seconds and straighten within 22-40 seconds in response to rapid RH changes (Figure S2, and ESI†). We estimated the porous silk's WR actuation energy densities by considering the maximum mechanical work done by the silk on the polyimide films at 10% RH (Figure 1b). Based on the curvature, the elastic energy (U) stored in the curved bilayer structure was calculated by[1,22]:

$$U = \frac{(E_1 I_1 + E_2 I_2) L}{R^2} \quad (1)$$

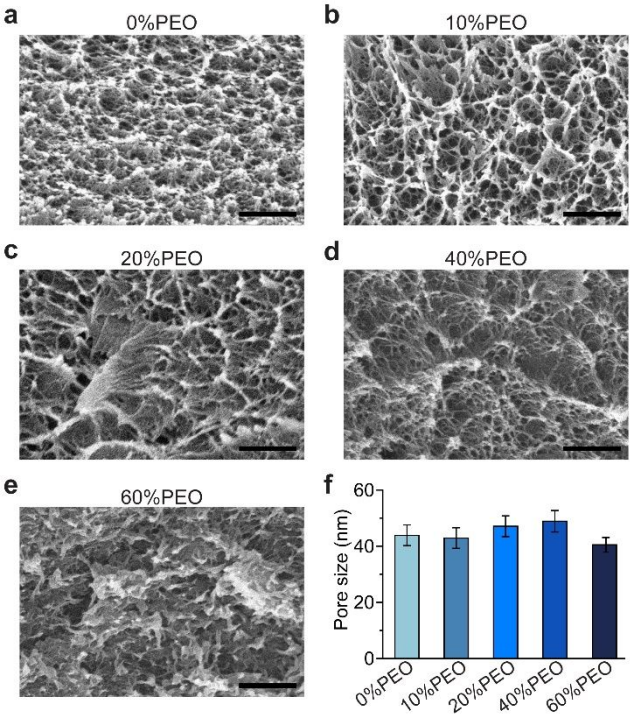

Figure 3. SEM cross-section images of *B. mori* silk films. a) 0%PEO, b) 10%PEO, c) 20%PEO, d) 40%PEO, and e) 60%PEO. Scale bar, 500 nm. f) Average pore diameters of porous silk. Error bars represent standard errors.

where R is the radius of the curved film measured using ImageJ, L is length of the polyimide film, I_1 and I_2 are the area moment of inertia of silk and polyimide layers, and E_1 and E_2 are Young's moduli of methanol-treated silk (~7.2 GPa)[1] and the polyimide substrate (2.5 GPa), respectively. Subsequently, the WR actuation energy density was calculated by dividing the elastic energy by the volume of the silk. We found that *B. mori* silk's energy density increases with increasing PEO concentrations but decreases when the PEO concentration is higher than 20% (Figure 1d). The energy density of silk with 20%PEO reaches 3,072 kJ m^{-3}, which is remarkably higher than those of previously reported water vapor annealed silk (487 kJ m^{-3}) or methanol treated silk (1626 kJ m^{-3}) [1]. This energy density also surpasses those of all known natural muscles[1], including mammalian muscles (8 kJ m^{-3}) [28]. However, the trend of WR actuation energy density does not directly correlate to the WR deformation (strain) as shown in Figure 1c. Comparing to WR strain, the significantly higher WR actuation energy of porous silk treated by 10% and 20% PEO suggest the higher WR actuation pressure of these samples.

To assess the porosity of silk and its effect on silk's water adsorption, we used dynamic water vapor sorption equipment (DVS Intrinsic Plus, Surface Measurement Systems) to measure the water sorption isotherms. To carry out the experiment, ~2 mg of freestanding porous silk films was placed on the ultra-sensitive microbalance. The mass change was continuously recorded throughout three consecutive RH cycles at 25°C. In each cycle, RH was increased from 10% to 90% and then decreased to 10% in 10% RH intervals. Before increasing to the next RH step, the mass change per unit time (dm/dt) ≤ 0.01 % min^{-1} was maintained for at least 10 min and the maximum time was fixed to be 90 min for each RH step. DVS analysis software (Advantage Advanced Analysis Suite, Surface Measurement Systems) was used to analyse the data (Figure S3, ESI†). The mass changes of silk and water sorption isotherms were obtained by comparing the mass of porous silk at different RHs to those at 10% RH, and maximum water adsorption was estimated by using Equation (2):

$$\text{Maximum water adsorption (\%)} = \frac{(m_{90\%\ RH} - m_{10\%\ RH})}{m_{10\%\ RH}} \times 100 \quad (2)$$

where $m_{90\%\ RH}$ and $m_{10\%\ RH}$ are equilibrium masses of *B. mori* silk at 90% and 10% RH measured by the DVS[1]. As shown in Figure 2a-e, the maximum water adsorption of porous silk increased from 16.9% for 0%PEO to 24.1% for 60%PEO. During the measurement, pores in silk mostly close at 10% RH, and then fully reopen after adsorb water at 90% RH. Thus, the total amount of water uptake by porous silk (maximum water adsorption) indicates the total volume of pores of silk under humid conditions. The increase in water uptake of porous silk

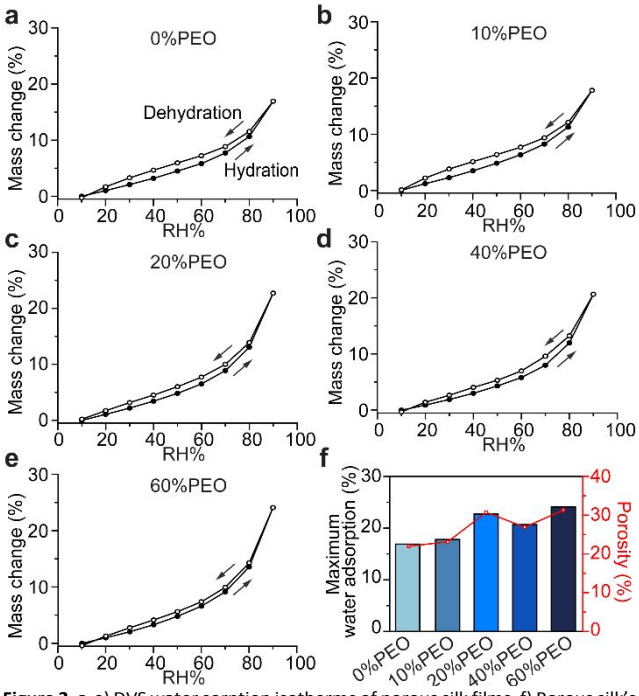

Figure 2. a-e) DVS water sorption isotherms of porous silk films. f) Porous silk's maximum water adsorption and porosities.

with increasing PEO concentrations clearly suggests the increase in porosity of PEO treated silk, which also agrees with the previously studies where PEO increases the porosity of silk[25,27]. To further quantify the porosity of silk, we analysed the volume ratio between adsorbed water and silk by considering their densities (*B. mori* silk density is 1.3 g/mL [29]), and found the porosity of silk to be: 22.0% for 0%PEO, 23.1% for 10%PEO, 29.5% for 20%PEO, 26.9% for 40%PEO, and 31.3% for 60%PEO (Figure 2f). Notably, the higher porosity correlates to the higher WR strain of silk treated by PEO with higher concentrations; however, it does not lead to higher WR actuation energy density (Figure 1c-d). We also note that all these water sorption isotherms show hysteresis between 20% RH and 80% RH, indicating a similar pore size distribution of the porous silk films (Figure 2a-e).

To visualize silk's porous structures, a scanning electron microscopy (SEM, Helios NanoLab 660) was used to take cross-section images of the porous silk. Before SEM imaging, porous silk films were teared and coated with a ~3 nm platinum layer using a sputter coater (Leica EM ACE600, Leica Microsystems). We found that all the silk films possess nanoporous structures (Figure 3). As shown in Figure 3a, methanol- and water-treated silk films without any PEO treatment show nanoporous structures, which agrees with previous studies that silk can form nanoscale pore structures after rinsing the silk fibroin matrix with water or organic solvents, such as ethanol or methanol[30]. PEO treated silk films also show nanoporous structures with circular-shaped nanoscale pore[26](Figure 3b-e). By analysing the SEM images using ImageJ (ESI†), we found that all silk treated by various PEO concentrations exhibits a similar pore size distribution of approximately 40 nm – 50 nm in diameter (43.9 nm (±3.69) for 0%PEO, 42.9 nm (±3.67) for 10%PEO, 47.1 nm (±3.7) for 20%PEO, 48.9 nm (±3.81) for 40%PEO, and 40.5 nm (±2.6) for 60%PEO) (Figure 3f), which agrees with previous observations that the pore size is mainly determined by the molecular weight of PEO[25,27]. These results, together with the water sorption isotherms, suggest that the difference in porous silk's strain and energy density is caused by the amount of pores and the connectivity of the pores, rather than pore size.

Our previous study shows that *B. mori* silk's water-responsiveness strongly correlates to its secondary structures, especially the silk II structure. We also studied the secondary structure changes of PEO treated silk by using attenuated total reflectance (ATR)-FTIR spectroscopy (Nicolet iS50 FTIR, Thermo Scientific) with a DTGS-KBr detector. For each sample, spectra were collected by accumulation of 32 scans with a resolution of 4 cm^{-1} between wavenumbers of 4000-400 cm^{-1}. In Figure 4a, the silk showed intense absorption peaks around 1625 cm^{-1}, which are characteristic of silk II structures (β-sheet crystal rich domain). To obtain the relative content of four secondary structures of β-sheet, random coil, α-helix, and β-turn, we deconvoluted the Amide I band (1710-1590 cm^{-1}) using the methods suggested by Qin et al.[31] For instance, we used four fixed representative peaks, including β-sheet (1625 cm^{-1}), random coil (1645 cm^{-1}), α-helix (1660 cm^{-1}), and β-turn (1678 cm^{-1}), and Gaussian distribution to fit the FTIR spectra (Figure S4). The deconvoluted FTIR data from each set of five samples

was then used to determine the average secondary silk protein structural contents for porous silk (Figure 4b). We found that the addition of PEO has a small effect on porous silk's secondary structures. For instance, 64.2% (± 1.12) β-sheet for 0%PEO, 64.5% (±0.69) β-sheet for 10%PEO, 65.1% (± 0.60) β-sheet for 20% PEO, 60.4% (± 1.02) β-sheet for 40%PEO, and 64.6% (± 0.82) β-sheet for 60% PEO. These results further confirm that the observed difference in porous silk's WR actuation is not a consequence of their secondary structures but rather the porosity of silk (Figure 2f).

To better understand the H-bonding network of the porous silk under humid and dry conditions, the OH stretching band of water was obtained by RH-dependent transmittance FTIR spectroscopy (Bruker VERTEX 70) and analysed. To carry out the experiment, the silk freestanding films were placed between two calcium fluoride glass disks within a customized RH-controlled chamber. Spectra were then collected with 64 scans and a resolution of 2 cm^{-1} between wavenumbers of 4000-1000 cm^{-1} at 10% and 90% RH. To compare the change of the OH stretching band with the PEO concentration, a wavenumber range of 3800-3000 cm^{-1} of was baseline corrected for all samples and normalized to unity (Figure 4c). The spectra were then smoothed before normalization through low-pass FFT filters by assigning cut-off frequency of ~0.03 (a.u.). Total peak area of the OH stretching band is known to increase linearly with water content[32]. We analysed the intensity difference of the OH stretching band of porous silk by comparing the peak areas at 90%RH to those at 10% by using Equation (3):

$$\text{Intensity difference}\ (\%) = \frac{(a_{90\%RH} - a_{10\%RH})}{a_{10\%RH}} \times 100 \quad (3)$$

where $a_{90\%RH}$ and $a_{10\%RH}$ are total peak area of the OH stretching band at 90% RH and 10% RH, respectively. Figure 4d shows that intensity difference increases linearly with PEO volume fractions. Comparing to other porous silk, the observed, relatively lower OH stretching intensity of the 20%PEO silk, together with the higher amount of water adsorption obtained by DVS (Figure 2f), suggest a higher percentage of mobilized water in 20%PEO silk adsorbed/desorbed during hydration/dehydration processes.

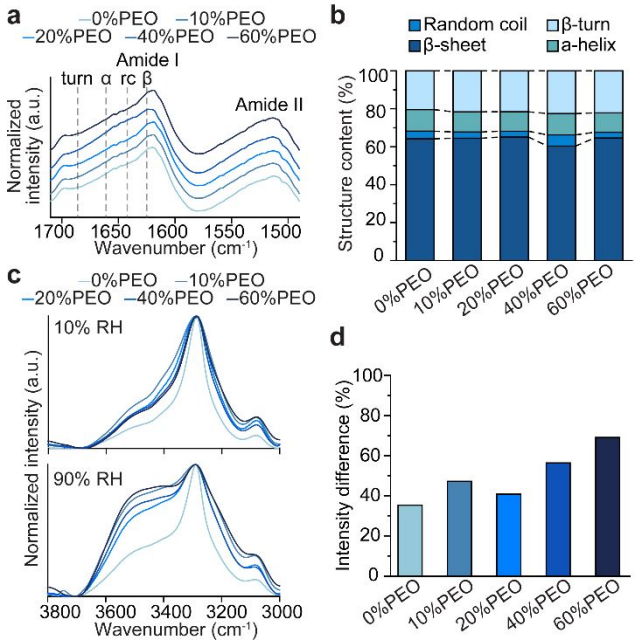

Figure 4. a) FTIR spectra of silk Amide I and II bands. b) Secondary structure contents calculated from the deconvoluted Amide I bands. c) OH stretching bands of water of porous silk films at 10% RH and 90% RH. d) Intensity difference of OH stretching bands at a function of PEO concentration.

We also noted that PEO treated silk films show higher peak intensities at wavenumbers of 3600-3400 cm^{-1} which is assigned for incomplete H-bonding network between water molecules[32-34], indicating that increasing in silk's porosity effects water-silk interactions and weaken the H-bonding network of water confined within silk's nanopores. Previous studies on peptide crystals[35] and peptidoglycan[2] have reported that materials' water-responsiveness correlates to their nanoconfined water's properties, such that enhanced H-bonding network will facilitate materials' WR power output. We expect that the optimal H-bonding network in 20%PEO silk can effectively transfer the pressure induced by chemical potential of water to open/close pores and deform silk's fibroins, which could also explain the higher amount mobilized water observed from the DVS (Figure 2f) and FTIR (Figure 4d). However, it is possible that when the silk has too much porosity, the increased incomplete H-bonding network would induce less viscous confined water within pores, reducing the pressure transferred to silk's macro structures.

Conclusions

In summary, we demonstrated that *B. mori* silk's water-responsiveness can be significantly enhanced by simply varying porosity of silk's nanoporous structures. Our studies suggest that porous silk's WR actuation energy density does not directly correlate to the water adsorption and WR strain but rather correlate to the nanoporosity and possibly the properties of nanoconfined water as a result of different porosities. Our findings of pore structure-dependent silk's water-responsiveness elucidate the potential approach of tuning the

porosity of silk, as well as other hygroscopic polymers, to develop scalable high-energy WR actuators.

Author Contributions

X.C., R.S.T., and Y.J. conceived and initiated the project. Y.J. and M.K. prepared the regenerated silk and porous silk films. Y.J. carried out bilayer curvature, ATR-FTIR, and DVS experiments and interpret the results. M.K. performed SEM and RH-controlled FTIR. D.P. assisted with RH control setup and FTIR analysis. T.S. carried out strain test. All authors contribute to the data analysis and the discussion of the results. Y.J., R.S.T. and X.C. wrote the paper.

Conflicts of interest

There are no conflicts to declare.

Acknowledgements

This work was supported in part by the Office of Naval Research (ONR) (N00014-18-1-8492 and N00014-22-1-2608), Air Force Office of Scientific Research (AFOSR) (FA9550-21-1-0144), and the Dr. Joan Eliasoph Fellows for Early Career STEM Researchers.

References

1 Y. Park, Y. Jung, T-D. Li, J. Lao, R. S. Tu and X. Chen, *Macromol. Rapid Commun.*, 2020, **41**, 1900612.
2 H. Wang, Z-L. Liu, J. Lao, S. Zhang, R. Abzalimov, T. Wang and X. Chen, *Adv. Sci.*, 2022, **9**, 2104697.
3 Y. Park and X. Chen, *J. Mater. Chem. A*, 2020, **8**, 15227-15244.
4 B. Shin, J. Ha, M. Lee, K. Park, G. H. Park, T. H. Choi, K-J. Cho and H-Y. Kim, *Sci. Robot.*, 2018, **3**, eaar2629.
5 K. Zhang, A. Geissler, M. Standhardt, S. Mehlhase, M. Gallei, L. Chen and C. M. Thiele, *Sci. Rep.*, 2015, **5**, 11011.
6 A. Holstov, B. Bridgens and G. Farmer, Constr. *Build. Mater.*, 2015, **98**, 570-582.
7 X. Chen, D. Goodnight, Z. Gao, A. H. Cavusoglu, N. Sabharwal, M. Delay, A. Driks and O. Sahin, *Nat. Commun.*, 2015, **6**, 7346.
8 H. Ma, X. Li, J. Lou, Y. Gu, Y. Zhang, Y. Jiang, H. Cheng and W. Han, *ACS Appl. Mater. Interfaces*, 2022, **14**, 3165–3175.
9 X. Jiang, B. Tian, X. Xuan, W. Zhou, J. Zhou, Y. Chen, Y. Lu and Z. Zhang, *Int. J. Smart Nano Mater.*, 2021, **12**, 146–156.
10 D. Reishofer, R. Resel, J. Sattelkow, W. J. Fischer, K. Niegelhell, T. Mohan, K. S. Kleinschek, H. Amenitsch, H. Plank, T. Tammelin, E. Kontturi and S. Spirk, *Biomacromolecules*, 2022, **23**, 1148–1157.
11 X. Chen, L. Mahadevan, A. Driks and O. Sahin, *Nat. Nanotechnol.*, 2014, **9**, 137-141.
12 N. A. Carter and T. Z. Grove, *J. Am. Chem. Soc.* 2018, **140**, 7144–7151.
13 J. Troyano, A. Carné-Sánchez and D. Maspoch, *Adv.Mater.*, 2019, **31**, 1808235.
14 J. Troyano, A. Carné-Sánchez, J. Pérez-Carvajal, L. León-Reina, I. Imaz, A. Cabeza and D. Maspoch, *Angew. Chem. Int. Ed.,* 2018, **57**, 15420–15424.
15 J. Mu, G. Wang, H. Yan, H. Li, X. Wang, E. Gao, C. Hou, A. T. C. Pham, L. Wu, Q. Zhang, Y. Li, Z. Xu, Y. Guo, E. Reichmanis, H. Wang and M. Zhu, *Nat. Commun.*, 2018, **9**, 590.
16 Y. Zhong, F. Zhang, M. Wang, C. J. Gardner, G. Kim, Y. Liu, J. Leng, S. Jin and R. Chen, *Sci. Rep.*, 2017, **7**, 44208.
17 M. Boudot, H. Elettro and D. Grosso, *ACS Nano*, 2016, **10**, 10031–10040.
18 X-L. Ye, L-Z. Liu and H-J. Jin, *Nanotechnology*, 2016, **27**, 325501.
19 M. Lee, G. Han and J. Lee, *Appl. Phys. Lett.*, 2019, **115**, 091601.
20 H. Kang, M. Lee, H. Lim, H. A. Stone and J. Lee, *NPG Asia Mater.*, 2017, **9**, 417.
21 L. Shen, J. Fu, K. Fu, C. Picart and J. Ji, *Langmuir*, 2010, **26**, 16634–16637.
22 Y. Jung, S. Sharifi Golru, T-D. Li, E. J. Biddinger, R. S. Tu and X. Chen, *Soft Matter*, 2021, **17**, 7817–7821.
23 M. Demura and T. Asakura, *J. Membr. Sci.*, 1991, **59**, 39-52.
24 Y. Wang, Z. Zheng, Q. Cheng, D. L. Kaplan, G. Li and X. Wang, *ACS Biomater. Sci. Eng.*, 2020, **6**, 1176–1185.
25 H-J. Jin, J. Park, R. Valluzzi, P. Cebe and D. L. Kaplan, *Biomacromolecules*, 2004, **5**, 711–717.
26 B. D. Lawrence, F. Omenetto, K. Chui and D. L. Kaplan, *J. Mater. Sci.*, 2008, **43**, 6967–6985.
27 S. Suzuki, R. Dawson, T. Chirila, A. Shadforth, T. Hogerheyde, G. Edwards and D. Harkin, *J. Funct. Biomater.,* 2015, **6**, 345-366.
28 P. Brochu and Q. Pei, *Macromol. Rapid Commun.,* 2010, **31**, 10–36.
29 H-P. Zhao, X-Q. Feng, and H-J. Shi, *Mater. Sci. Eng. C,* 2007, **27**, 675.
30 F. Zhang, R. Yang, P. Zhang, J. Qin, Z. Fan and B. Zuo, *ACS Omega*, 2019, **4**, 3114–3121.
31 N. Qin, S. Zhang, J. Jiang, S. G. Corder, Z. Qian, Z. Zhou, W. Lee, K. Liu, X. Wang, X. Li, Z. Shi, Y. Mao, H. A. Bechtel, M. C. Martin, X. Xia, B. Marelli, D. L. Kaplan, F. G. Omenetto, M. Liu and T. H. Tao, *Nat. Commun.*, 2016, **7**, 13079.
32 J. B. Brubach, A. Mermet, A. Filabozzi, A. Gerschel, D. Lairez, M. P. Krafft and P. Roy, *J. Phys. Chem. B.*, 2001, **105**, 430–435.
33 F. Cheng, Q. Cao, Y. Guan, H. Cheng, X. Wang and J. D. Miller, *Int. J. Miner. Process.*, 2013, **122**, 36–42.
34 A. Vasylieva, I. Doroshenko, Y. Vaskivskyi, Y. Chernolevska and V. Pogorelov, *J. Mol. Struct.*, 2018, **1167**, 232–238.
35 R. Piotrowska, T. Hesketh, H. Wang, A. R. G. Martin, D. Bowering, C. Zhang, C. T. Hu, S. A. McPhee, T. Wang, Y. Park, P. Singla, T. McGlone, A. Florence, T. Tuttle, R. v. Ulijn and X. Chen, *Nat. Mater.,* 2021, **20**, 403-409.